JGR Solid Earth

RESEARCH ARTICLE
10.1029/2019JB017500

Influence of Grain Boundary Structural Evolution on Pressure Solution Creep Rates

M. P. A. van den Ende[1,2], A. R. Niemeijer[1], and C. J. Spiers[1]

[1]High Pressure and Temperature Laboratory, Department of Earth Sciences, Utrecht University, Utrecht, The Netherlands, [2]Now at Université Côte d'Azur, IRD, CNRS, Observatoire de la Côte d'Azur, Géoazur, Nice, France

Key Points:
- A new model is presented for the structural evolution of stressed grain boundaries undergoing pressure solution
- This model is tested against laboratory single-contact and granular aggregate compression tests
- The model reconciles classical pressure solution theory with laboratory observations of aggregate compaction at low porosities

Correspondence to:
M. P. A. van den Ende,
martijn.vandenende@geoazur.unice.fr

Citation:
van den Ende, M. P. A., Niemeijer, A. R., & Spiers, C. J. (2019). Influence of grain boundary structural evolution on pressure solution creep rates. *Journal of Geophysical Research: Solid Earth*, *124*, 10,210–10,230. https://10.1130/10.1029/2019JB017500

Received 4 FEB 2019
Accepted 9 SEP 2019
Accepted article online 11 SEP 2019
Published online 24 OCT 2019

Abstract Intergranular pressure solution is a well-known rock deformation mechanism in wet regions of the upper crust and has been widely studied, especially in the framework of compaction of granular materials, such as reservoir sandstones and fault rocks. Several analytical models exist that describe compaction creep by stress-induced mass transport, and the parameters involved are relatively well constrained by laboratory experiments. While these models are capable of predicting compaction behavior observed at relatively high porosities, they often overestimate compaction rates at porosities below 20% by up to several orders of magnitude. This suggests that the microphysical processes operating at low porosities are different and are not captured well by existing models. The implication is that available models cannot be extrapolated to describe compaction of sediments and fault rocks to the low porosities often reached under natural conditions. To address this problem, we propose a new, thermodynamic model that describes the decline of pressure solution rates within individual grain contacts as a result of time-averaged growth of asperities or islands and associated constriction of the grain boundary diffusion path (here termed grain boundary evolution). The resulting constitutive equations for single grain-grain contacts are then combined and solved semianalytically. The compaction rates predicted by the model are compared with those measured in high-strain compaction experiments on wet granular halite. A significant reduction in compaction rate is predicted when grain boundary evolution is considered, which compares favorably with the experimental compaction data.

1. Introduction

Intergranular pressure solution, or dissolution-precipitation creep, is an important mechanism of time-dependent deformation of rocks under wet, upper-crustal conditions (Lehner, 1990; Rutter & Elliott, 1976; Spiers et al., 1990, 2004). Its relevance is recognized, in particular, in relation to the compaction of granular rock materials (Croizé et al., 2010; Gratier, 1987; Karner et al., 2003; Spiers & Schutjens, 1990; Tada & Siever, 1989), in shear deformation of dense rocks under greenschist and blueschist metamorphic conditions (Elliott, 1973; Stöckhert et al., 1999), and in controlling the frictional behavior and strengthening of faults (Blanpied et al., 1992; Bos et al., 2000; Jefferies et al., 2006; Karner et al., 1997; Niemeijer & Spiers, 2006). Crucial for the operation of pressure solution is the presence of a grain boundary solution phase in the form of an adsorbed thin film (Robin, 1978; Rutter, 1983) or of a dynamically stable island-channel structure (Lehner, 1990; Raj, 1982; Spiers & Schutjens, 1990). Numerous models have been developed to describe the microscale processes that operate during pressure solution (e.g., Lehner, 1990; Shimizu, 1995; Spiers et al., 1990), and the constitutive parameters involved have been constrained in a range of different laboratory experiments (e.g., Dewers & Hajash, 1995; Gratier et al., 2009; Raj, 1982; Rutter & Elliott, 1976; Spiers et al., 1990; van Noort et al., 2008). However, many experimental studies investigating compaction by pressure solution consider time scales that are insufficient to reach low porosities (<20%), being limited by the relatively slow kinetics of the process. Studies in which low porosities are achieved report compaction rates that fall orders of magnitude below values that are predicted by analytical models for pressure solution creep (Niemeijer et al., 2002; Schutjens, 1991).

This discrepancy exposes an important shortcoming in our understanding of the microscale processes at play and limits our ability to reliably extrapolate laboratory results to nature. As an example, observations of a terminal porosity as seen in sedimentary basins (e.g., Ramm, 1992), indicating an (apparent) equilibrium state, challenge classical views that treat pressure solution as a nonequilibrium process (Lehner & Bataille, 1985). Aside from the scientific conundrum, the uncertainty in the long-term basin dynamics has immediate implications for, for example, hydrocarbon production and wastewater disposal. In the context of fault rock

deformation and earthquake cycles, time-dependent fault zone restrengthening and fluid pressure buildup in faults have been proposed to result from compaction by pressure solution creep (Angevine et al., 1982; Sleep & Blanpied, 1992). Estimates of long-term (centennial) fault zone restrengthening accordingly require accurate descriptions of pressure solution creep over the full range of attainable fault rock porosities. As a candidate mechanism for the retardation (and possibly arrest) of pressure solution at low porosities, sealing/healing of grain boundaries due to surface energy-driven mass transfer has been suggested (Hickman & Evans, 1991; van Noort et al., 2008; Visser, 1999). Crack and grain boundary healing or sealing, driven by surface energy reduction, has similarly been suggested as a mechanism for fault rock restrengthening (Beeler & Hickman, 2015; Brantley, 1992; Hickman & Evans, 1992).

Here, we develop analytical expressions that describe the evolution of grain boundary structure during deformation by pressure solution and its effect on the rate of pressure solution. To validate the model, we compare the predicted compaction rates with laboratory data on compression of halite-glass interfaces (Renard et al., 2012) and on compaction of granular halite provided by Schutjens (1991). We find that grain boundary evolution involving increasing solid-solid contact area with time can readily explain growth of contact asperities as observed by Renard et al. (2012) and the reduction in strain rate observed by Schutjens (1991). Agreement between model and experiment is improved further if the thickness of the grain boundary zone is allowed to increase with increasing grain contact length scale, following a fractal scaling relationship.

2. Previous Work on Pressure Solution and Grain Boundary Healing

2.1. Pressure Solution in Theory and Experiment

In general, pressure solution in a porous rock system where there is no long-range mass transport can be seen as a series of three consecutive processes: (1) dissolution of material at stressed grain-grain contacts, (2) diffusion of the dissolved mass out of the grain contact zone, and (3) precipitation on the pore walls. Which of these serial processes control the overall rate of pressure solution is determined by kinetics of dissolution, diffusion, and precipitation, respectively. When it is assumed that only the rate of ionic diffusion limits the kinetics of pressure solution (as is commonly the case for highly soluble materials like alkali metal salts; Niemeijer et al., 2002; Spiers et al., 2004), then for the case of either 1-D or isotropic compaction, the macroscopic strain rate can be described by the following analytical expression (Pluymakers & Spiers, 2015; Rutter & Elliott, 1976; Shimizu, 1995; Spiers & Schutjens, 1990):

$$\dot{\varepsilon} = A_\varepsilon \frac{(DCS)\Omega}{RT}\frac{\sigma_e}{d^3} f(\phi) \tag{1}$$

Here, $\dot{\varepsilon}$ represents the volumetric strain rate, A_ε a geometric constant, d the mean grain size, σ_e the effective stress (applied axial stress or confining pressure minus pore fluid pressure), Ω the molar volume of the solid, R the universal gas constant, T the absolute temperature, D the effective diffusion coefficient of the ionic species dissolved in the grain boundary fluid, C the solubility of a flat, unstressed solid interface, S the (mean) thickness of fluid in the grain boundary zone, and $f(\phi)$ a dimensionless function of porosity (ϕ) which accounts for the evolution of contact area and pore wall area during compaction. The rate coefficient for diffusion within the grain boundary (DCS) varies with temperature and exhibits an Arrhenius dependence on temperature, that is, takes the form (e.g., Spiers et al., 1990; Spiers & Schutjens, 1990):

$$(DCS) = (DCS)_0 \exp\left(-\frac{\Delta H}{RT}\right) \tag{2}$$

with ΔH being the apparent activation energy associated with diffusion within the grain boundary.

As mentioned above, the kinetics of diffusion-controlled pressure solution are governed by the combined product DCS. This parameter encompasses the structure of the grain boundary through the effective cross section (mean fluid thickness) and the effects of any surface force interactions between the solid, the fluid, and the dissolved ionic species. Effects of grain boundary diffusion path tortuosity can be accounted for by replacing D with an effective value of D. For steady-state pressure solution, many analytical models assume a dynamically stable island-channel grain boundary structure (Lehner, 1990; Raj, 1982; Spiers & Schutjens, 1990), in which contact asperities and surrounding grain boundary interfaces undergo continuous dissolution and precipitation. In this way, the grain boundary does not attain thermodynamic equilibrium but is expected to evolve into a dynamically rough structure with time-stationary statistical properties (Lehner, 1990), as has

been observed in many laboratory experiments (de Meer et al., 2002, 2005; Renard et al., 2012; Schutjens & Spiers, 1999). However, the assumption of a steady-state grain boundary structure may be violated when the stresses on the grain-grain contacts decrease and surface energy driving forces start to play a role in controlling the energy balance within the grain boundary (Schutjens & Spiers, 1999; van Noort et al., 2008; Visser, 1999). Several experiments (e.g., Schutjens & Spiers, 1999) have shown that the grain boundary structure is rough and open at high effective contact stress and much more constricted at low effective stress, indicating an evolution in grain boundary structure with decreasing contact stress. It is therefore expected that the product *DCS* is lower in low porosity aggregates (i.e., low contact stress) than at high porosity.

2.2. Thermodynamics of Grain Boundary Healing and Sealing

In order to further comprehend the evolution of grain contacts under stress, we will now review basic thermodynamic concepts that are prerequisites for developing a model for grain boundary structural change during compaction by pressure solution.

The chemical equilibrium at a triple junction between two grains of an isotropic solid plus a fluid phase can be described by the Young-Dupré relation (e.g., Holness, 1992):

$$\gamma_{ss} = 2\gamma_{sl}\cos\left(\frac{\theta_{eq}}{2}\right) \tag{3}$$

Here, γ_{sl} and γ_{ss} denote the solid-liquid and solid-solid interfacial energy, respectively, and θ_{eq} denotes the dihedral angle at equilibrium. It was shown by *Visser* and coworkers (van Noort et al., 2008; Visser, 1999) that when the dihedral angle θ at the contact margin deviates from the equilibrium value θ_{eq}, a thermodynamic force F (N/m) is exerted on the contact margin, given by:

$$F = 2\gamma_{sl}\left(\cos\frac{\theta}{2} - \cos\frac{\theta_{eq}}{2}\right) = 2\gamma_{sl}\Delta\cos\frac{\theta}{2} \tag{4}$$

This force may drive lateral spreading (neck growth) or retreat (marginal dissolution or undercutting) of the solid-solid contact. A dynamically wetted island-channel structure represents a nonequilibrium state, and as such is an elevated energy state. This elevated state is thought to be maintained by local stress-induced perturbations that may overcome any surface energy reduction effects (Lehner, 1990; Spiers & Schutjens, 1990; Visser, 1999). However, if the stress on the grain contact is removed or is reduced below a threshold value at which the local stress perturbations are insufficient to maintain a dynamically wetted state, the solid-liquid interfaces within a grain boundary will reconfigure toward a configuration of disconnected pockets of fluids that (locally) minimizes the interfacial and total energy content of the grain boundary. In the case of static growth of the asperities, this process is referred to as *grain boundary healing* (van Noort et al., 2008; Visser, 1999).

Following Visser (1999) and van Noort et al. (2008), one can express the potential for lateral growth of stressed asperities within a grain-grain contact in terms of a competition between the effects of the applied stress on the elastic strain energy f_{el} and surface energy. In this treatment, the asperities are viewed as small, dynamically migrating islands with constant height and a dynamic dihedral angle of θ=0. Then, the chemical potential $\Delta\mu_i$ (units: J/m^3) for lateral growth at low fluid pressures compared to the effective stress is expressed as (van Noort et al., 2008) :

$$\Delta\mu_i = \frac{F}{S} - \Delta f_{el} = \frac{2\gamma_{sl}}{S}\Delta\cos\frac{\theta}{2} - \frac{(\sigma_c/\alpha)^2}{2E} \tag{5}$$

Here, Δf_{el} is the difference between the average value of f_{el} from the stressed island to the grain contact margin, σ_c denotes the mean effective normal stress on the grain contact scale (i.e., $\sigma_n - P_f$), α the relative asperity area fraction, and E the Young's modulus. If $\Delta\mu_i$>0, lateral growth of the asperities occurs, driven by the surface energy force F (first term in the right-hand side of the equality), dominating over Δf_{el} (second term in the right-hand side). If $\Delta\mu_i$<0, nett dissolution occurs due to dominance of the stored elastic energy Δf_{el}. The criterion for static island growth, hence grain boundary healing, is then defined by the condition $\Delta\mu_i$>0, so that the critical effective stress σ_{crit} below which healing occurs can be written in terms of the equilibrium condition:

$$\sigma_{\text{crit}} = 2\alpha\sqrt{E\frac{\gamma_{\text{sl}}}{S}\Delta\cos\frac{\theta}{2}} \tag{6}$$

For effective contact stresses lower than σ_{crit}, it is expected that the surface energy term in equation (5) dominates and that nett growth of the asperities results in healing of the grain boundary. This criterion subdivides the dynamic wetting versus grain boundary healing fields but does not provide information regarding the rateof asperity growth in a transient state, in either stressed (pressure dissolving) or unstressed grain contacts. To gain more insight into the interplay between structural evolution of grain boundaries and compaction by pressure solution, we propose a new model below.

3. Microphysical Model for the Effects of Grain Boundary Structural Change on Pressure Solution

3.1. Grain Boundary Evolution Model

Following Lehner (1990), the grain boundary zone during pressure solution is envisioned to consist of a dynamically rough topography of contact asperities (islands) that are separated by a continuous, interconnected network of interstitial fluid (channels)—see Figure 1. In previous studies deriving expressions for steady-state pressure solution creep, it is generally assumed that the island-channel network is a steady-state structure of which the properties, averaged over the entire grain boundary, remain constant over time (Lehner, 1990; Raj, 1982; Spiers & Schutjens, 1990). Similarly, we assume the average height of the grain boundary topography (S) to be time invariant. The total area of the grain contact A_c that is occupied by islands (i.e., solid-solid contacts) is denoted by A_{ss}. The contact area A_c increases as grain-to-grain convergence proceeds by pressure solution. It is convenient to define the relative island occupation ratio as $\alpha \equiv A_{\text{ss}}/A_c$. From this definition it follows that the area occupied by channels A_{sl} is $(1-\alpha)A_c$. During active pressure solution creep, mass is transported through the grain boundary peripheral area A_p by a diffusive flux J_p, which is defined positive when directed outward from the grain boundary into the pore space. Similarly, when the grain boundary area occupied by islands increases (i.e., when α increases), fluid is expelled out of the grain boundary, defining a positive advective flux Q_p, carrying a mean solute concentration $\bar{C}$.

Let us now consider a single disc-shaped contact between two cylindrical grains with depictions and assumptions given in Figure 1 (specifically Figures 1b–1d). During active pressure solution with island growth, and assuming constant solid density, the mass/volume balance for the solid in the cylindrical, two-grain contact is given by:

$$\begin{aligned} 2A_cV_{ps} = A_pJ_p + \bar{C}\,Q_p + \frac{\mathrm{d}(A_{\text{ss}}S)}{\mathrm{d}t} + \frac{\mathrm{d}(\bar{C}A_{\text{sl}}S)}{\mathrm{d}t} &= A_pJ_p + A_cS\bar{C}\frac{\mathrm{d}\alpha}{\mathrm{d}t} + A_cS\frac{\mathrm{d}\alpha}{\mathrm{d}t} \\ &\quad + A_c(1-\alpha)S\frac{\mathrm{d}\bar{C}}{\mathrm{d}t} - A_cS\bar{C}\frac{\mathrm{d}\alpha}{\mathrm{d}t} \approx A_pJ_p + A_cS\frac{\mathrm{d}\alpha}{\mathrm{d}t} \end{aligned} \tag{7}$$

In the first line of this equation, the different terms represent, in order, mass dissolved from the grain contact by pressure solution, the diffusive and advective mass fluxes through the grain contact periphery, respectively, the solid mass stored in the islands, and the mass stored as dissolved species in the channels (all in units of cubic meters per second). We neglect minor changes occurring in the mean solid concentration $\bar{C}$ in the grain boundary fluid. By noting that all solid volume expelled from the contact (A_pJ_p) will be precipitated on the free grain or pore walls when diffusion is rate controlling and that the fluid volume expelled from the grain contact must equal the increase in grain boundary island volume ($A_cS\dot{\alpha}$), the fluid volume v^f displaced against the fluid pressure P_f must be

$$\frac{\mathrm{d}v^f}{\mathrm{d}t} = A_pJ_p + A_cS\frac{\mathrm{d}\alpha}{\mathrm{d}t} = 2A_cV_{ps} \tag{8}$$

Following Lehner, (1990, 1995), the energy/entropy balance for the two-grain system represented in Figure 1b, neglecting contributions related to minor changes in solute concentration in the fluid phase, can be written as follows:

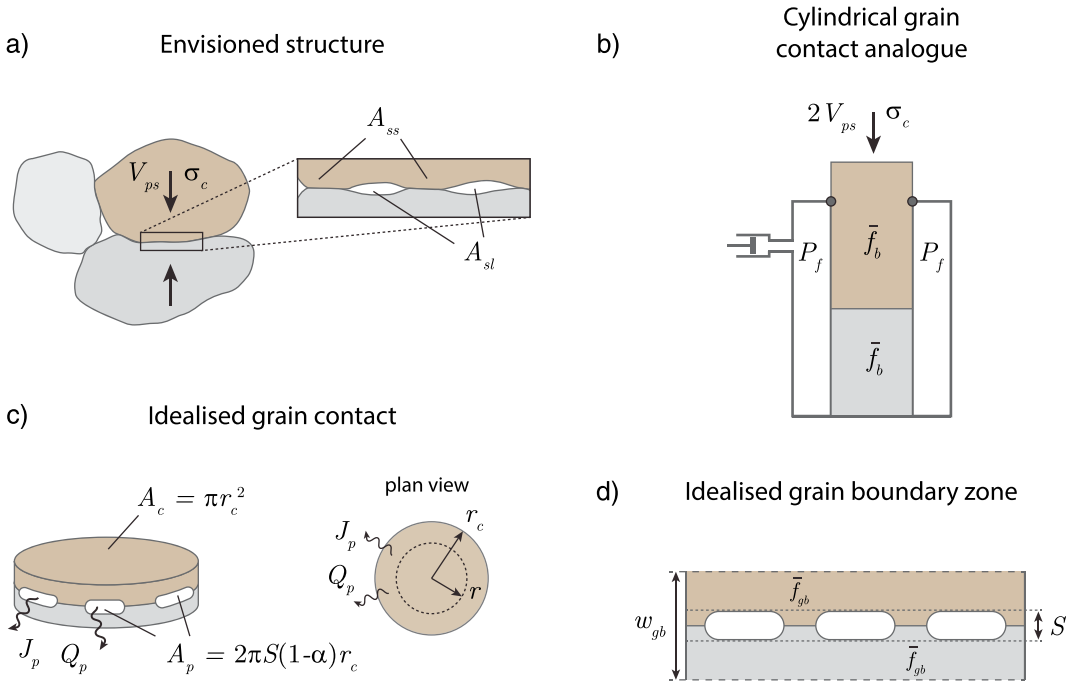

Figure 1. Synopsis of the grain geometries adopted in this work. (a) During pressure solution, the envisioned grain contacts exhibit a dynamically stable island-channel structure (cf. Lehner, 1990), in which the total cross-sectional area of solid-solid contact points (the islands) is A_{ss}, and the total cross-sectional area that is open to the interstitial fluid (the channels) is A_{sl}. (b) In deriving the analytical constitutive relations, a cylindrical grain geometry is assumed, here represented by an analog of a 2-D cross section of two cylindrical grains. The solid framework is submersed in a fluid of constant pressure P_f and loaded axially with an effective stress σ_c, which raises the mean-free energy density of each grain to $\bar{f}_b$ and causes convergence at a rate $2V_{ps}$. (c) The grain contact is envisioned as a disc-shaped region of thickness w_{gb}, cross-sectional area A_c, and radius r_c. Mass is transported out of the grain contact region through the open periphery A_p.(d)Within the grain boundary region, the solid has a mean-free energy density $\bar{f}_{gb}$. The average height of the islands and channels is denoted by S.

$$\dot{W} = \dot{F} + \dot{E}_s + \dot{\Delta} \tag{9}$$

where $\dot{W}$ is the mechanical work input rate, $\dot{F}$ is the rate of increase of Helmholtz energy of the solid phase, $\dot{E}_s$ accounts for the changes in surface stored energy caused by island growth/contraction, and $\dot{\Delta} \geq 0$ is the rate of dissipation due to irreversible processes (all in units of Joules per second).

For the nett work input rate, we can write (using equations (7) and (8)):

$$\dot{W} = 2\sigma_c A_c V_{ps} - P_f \frac{\mathrm{d}\nu^f}{\mathrm{d}t} = 2\left[\sigma_c - P_f\right] A_c V_{ps} \tag{10}$$

For $\dot{F}$, we can write $\dot{F} = \dot{F}_b + \dot{F}_{gb}$, that is, as the sum of the energy changes occurring in the grain bodies ($\dot{F}_b$) and the solid portion of the grain boundary zone ($\dot{F}_{gb}$). Here, $\dot{F}_b$ is the energy change due to mass removal from the grain bodies ($-2\bar{f}_b A_c V_{ps}$), plus the energy stored in mass precipitation on the pore walls ($+2\bar{f}_b A_p J_p$), so that, using equation (7), we get:

$$\frac{\mathrm{d}F_b}{\mathrm{d}t} = \bar{f}_b\left(A_p J_p - 2A_c V_{ps}\right) = -\bar{f}_b A_c S \frac{\mathrm{d}\alpha}{\mathrm{d}t} \tag{11}$$

where $\bar{f}_b$ is the mean-free energy density of solid stored in the grain body (units: J/m^3). In turn

$$\frac{\mathrm{d}F_{gb}}{\mathrm{d}t} = \frac{\mathrm{d}\left(\bar{f}_{gb}\nu^s_{gb}\right)}{\mathrm{d}t} = \bar{f}_{gb}\frac{\mathrm{d}\nu^s_{gb}}{\mathrm{d}t} + \nu^s_{gb}\frac{\mathrm{d}\bar{f}_{gb}}{\mathrm{d}t} \tag{12}$$

where $\bar{f}_{gb}$ is the mean-free energy density of the solid in the perturbed grain boundary zone and ν^s_{gb} is the volume of solid in the grain boundary zone. Clearly, from Figure 1d, $\nu^s_{gb} = A_c S\alpha$. Using this relation, we combine equations (11)and (12) to give:

$$\frac{\mathrm{d}F}{\mathrm{d}t}=\frac{\mathrm{d}F_b}{\mathrm{d}t}+\frac{\mathrm{d}F_{\mathrm{gb}}}{\mathrm{d}t}=\left(\bar{f}_{\mathrm{gb}}-\bar{f}_b\right)A_cS\frac{\mathrm{d}\alpha}{\mathrm{d}t}+\nu^s_{\mathrm{gb}}\frac{\mathrm{d}\bar{f}_{\mathrm{gb}}}{\mathrm{d}t} \tag{13}$$

The first term on the right-hand side represents the excess solid energy stored in the grain boundary zone as the islands grow in volume, and the second corresponds to the change in grain boundary solid energy due to changing stress/strain concentrations in the evolving grain boundary structure.

The interfacial energy stored in the grain boundary zone is simply the sum $E_s=\gamma_{\mathrm{ss}}A_c\alpha+2\gamma_{\mathrm{sl}}A_c(1-\alpha)$ of solid-solid (*ss*) and solid-liquid (*sl*) interfacial energy (γ) terms (factor of 2 accounting for the solid-liquid interfaces on both sides of the contact). This means that

$$\dot{E}_s=\gamma_{\mathrm{ss}}A_c\frac{\mathrm{d}\alpha}{\mathrm{d}t}-2\gamma_{\mathrm{sl}}A_c\frac{\mathrm{d}\alpha}{\mathrm{d}t}=(\gamma_{\mathrm{ss}}-2\gamma_{\mathrm{sl}})A_c\frac{\mathrm{d}\alpha}{\mathrm{d}t} \tag{14}$$

The solid-solid and solid-liquid surface energy terms are then related through the Young-Dupré relation (Holness, 1992) as given in equation (3):

$$\gamma_{\mathrm{ss}}=2\gamma_{\mathrm{sl}}\cos\frac{\theta_{\mathrm{eq}}}{2} \tag{15}$$

Substitution of this relation into equation (14) gives the following:

$$\dot{E}_s=-2\gamma_{\mathrm{sl}}\left(1-\cos\frac{\theta_{\mathrm{eq}}}{2}\right)A_c\frac{\mathrm{d}\alpha}{\mathrm{d}t}=-2\gamma_{\mathrm{sl}}\Delta\cos\frac{\theta}{2}A_c\frac{\mathrm{d}\alpha}{\mathrm{d}t} \tag{16}$$

Note that the definition of $\Delta\cos(\theta/2)$ is equivalent to that of Visser (1999) as given in equation (4) when $\theta=0$, which is in full agreement with the idealized grain boundary geometry displayed in Figure 1d.

From equation (9), we hence obtain for the total dissipation:

$$\dot{\Delta}=\dot{W}-\dot{F}-\dot{E}_s=2\left[\sigma_c-P_f\right]A_cV_{ps}+\left[\frac{2\gamma_{\mathrm{sl}}}{S}\Delta\cos\frac{\theta}{2}-\left(\bar{f}_{\mathrm{gb}}-\bar{f}_b\right)\right]A_cS\frac{\mathrm{d}\alpha}{\mathrm{d}t}-\nu^s_{\mathrm{gb}}\frac{\mathrm{d}\bar{f}_{\mathrm{gb}}}{\mathrm{d}t} \tag{17}$$

During active pressure solution with negligible inelastic deformation of the solid framework, this dissipation will be caused by the internal grain contact mass transfer process. Assuming that the rate of mass transfer is controlled by diffusion, then the dominant dissipative process will be radial grain boundary diffusion, with any internal short range diffusional dissipation being negligible. Hence, we can express the rate of dissipation for a radial increment dr due to radial diffusion as (Lehner, 1990; Pluymakers & Spiers, 2015) follows:

$$\mathrm{d}\dot{\Delta}=-J_ra_p\frac{\partial\mu}{\partial r}\mathrm{d}r \tag{18}$$

where $a_p=2(1-\alpha)S\pi r$ is the peripheral area at radius r that is open to the radial diffusive flux J_r. The diffusive flux is driven by a gradient in chemical potential μ, as given by Fick's first law:

$$J_r=-\frac{DC\Omega}{RT}\frac{\partial\mu}{\partial r} \tag{19}$$

Rewriting the solid mass balance equation (7) for a grain boundary element explicitly for the diffusive flux and substituting equation (19) gives the following:

$$\begin{aligned}J_r&=\frac{a_c}{a_p}\left(2V_{ps}-S\frac{\mathrm{d}\alpha}{\mathrm{d}t}\right)=-\frac{DC\Omega\partial\mu}{RT\ \partial r}\\ \Rightarrow\frac{\partial\mu}{\partial r}&=-\frac{RT\ a_c}{DC\Omega a_p}\left(2V_{ps}-S\frac{\mathrm{d}\alpha}{\mathrm{d}t}\right)\end{aligned} \tag{20}$$

with $a_c=\pi r^2$ at radius r. Substituting equation (20) into (18) and integrating over the grain contact area gives the final expression for $\dot{\Delta}$:

$$\Delta\dot{} = \frac{DC\Omega}{RT}\int_0^{r_c} a_p\left(\frac{\partial\mu}{\partial r}\right)^2 \mathrm{d}r = \frac{\pi}{2}\frac{RT}{DCS1-\alpha\Omega}\left(2V_{ps}-S\frac{\mathrm{d}\alpha}{\mathrm{d}t}\right)^2\int_0^{r_c} r^3\mathrm{d}r = A_c\frac{r_c^2}{8}\frac{RT}{DCS1-\alpha\Omega}\left(2V_{ps}-S\frac{\mathrm{d}\alpha}{\mathrm{d}t}\right)^2 \quad (21)$$

Combining equations (17) and (21), and noting from Figure 1d that $v_{\mathrm{gb}}^s = \left[w_{\mathrm{gb}}-(1-\alpha)S\right]A_c$ (w_{gb} being the width of the grain boundary zone), now leads to the result:

$$2\left[\sigma_c-P_f\right]V_{ps} + \left[\frac{2\gamma_{\mathrm{sl}}}{S}\Delta\cos\frac{\theta}{2}-\left(\overline{f}_{\mathrm{gb}}-\overline{f}_b\right)\right]S\frac{\mathrm{d}\alpha}{\mathrm{d}t}- \left[w_{\mathrm{gb}}-(1-\alpha)S\right]\frac{\mathrm{d}\overline{f}_{\mathrm{gb}}}{\mathrm{d}t} = \frac{r_c^2}{8}\frac{RT}{DCs(1-\alpha)\Omega}\left(2V_{ps}-S\frac{\mathrm{d}\alpha}{\mathrm{d}t}\right)^2 \quad (22)$$

Assuming that the grain boundary zone is thin, so that $w_{\mathrm{gb}}\rightarrow S$, it is reasonable to suppose that the main contribution to the excess free energy density in the grain boundary solid over the grain bodies, that is, to $\left(\overline{f}_{\mathrm{gb}}-\overline{f}_b\right)$, will be provided by the strain energy f_i stored in the highly loaded grain boundary islands. Taking this to be dominated by the elastic strain energy, we can write (cf. van Noort et al., 2008) the following:

$$\left(\overline{f}_{\mathrm{gb}}-\overline{f}_b\right)\approx f_i = \frac{1}{2E}\left(\frac{\sigma_c}{\alpha}\right)^2 \quad (23)$$

where E is the Young's modulus of the solid. Writing $\overline{f}_{\mathrm{gb}}\approx f_i+\overline{f}_b$ and noting that $\overline{f}_b$, the free energy density in the grain bodies, is constant at constant σ_c, it follows for $\mathrm{d}\overline{f}_{\mathrm{gb}}/\mathrm{d}t$ in equation (22) that:

$$\frac{\mathrm{d}\overline{f}_{\mathrm{gb}}}{\mathrm{d}t} = \frac{\mathrm{d}f_i}{\mathrm{d}t} = \frac{\sigma_c^2}{2E}\frac{\mathrm{d}(\alpha^{-2})}{\mathrm{d}t} = -\frac{\sigma_c^2}{E}\frac{1}{\alpha^3}\frac{\mathrm{d}\alpha}{\mathrm{d}t} \quad (24)$$

Putting these relations for $\left(\overline{f}_{\mathrm{gb}}-\overline{f}_b\right)$ and $\mathrm{d}\overline{f}_{\mathrm{gb}}/\mathrm{d}t$ into (22) and taking $w_{\mathrm{gb}}\approx S$ now yields:

$$2\left[\sigma_c-P_f\right]V_{ps} + \left[\frac{2\gamma_{\mathrm{sl}}}{S}\Delta\cos\frac{\theta}{2}+\frac{1}{2E}\left(\frac{\sigma_c}{\alpha}\right)^2\right]S\frac{\mathrm{d}\alpha}{\mathrm{d}t} = \frac{r_c^2}{8}\frac{RT}{DCS(1-\alpha)\Omega}\left(2V_{ps}-S\frac{\mathrm{d}\alpha}{\mathrm{d}t}\right)^2 \quad (25)$$

For the steady-state case, when there is no evolution in grain boundary structure ($\dot{\alpha}=0$), this relation reduces to the standard equation for pressure solution convergence velocity at a cylindrical grain contact (Pluymakers & Spiers, 2015):

$$V_{ps} = \frac{4DCS(1-\alpha)\Omega}{RTr_c^2}\left[\sigma_c-P_f\right] \quad (26)$$

When the pressure solution rate slows down to approach zero due to obstruction of radial diffusion with increasing α, that is as $V_{ps}\rightarrow 0$, equation (25) reduces to

$$S\frac{\mathrm{d}\alpha}{\mathrm{d}t} = \frac{8DCS(1-\alpha)\Omega}{RTr_c^2}\left[\frac{2\gamma_{\mathrm{sl}}}{S}\Delta\cos\frac{\theta}{2}+\frac{1}{2E}\left[\frac{\sigma_c}{\alpha}\right]^2\right] \quad (27)$$

which expresses the rate of increase in contact area fraction occupied by islands of solid-solid contact under nonequilibrium conditions (compared with the condition for removal of an equilibrium grain boundary structure from equilibrium given by van Noort et al., 2008). Note that equation (27) describes the rate of island area increase during active pressure solution. The onset of static island growth is still described by the equilibrium condition given by van Noort et al. (2008) as follows:

$$\Delta\mu_i = \frac{2\gamma_{sl}}{S}\Delta\cos\frac{\theta}{2} - \frac{1}{2E}\left(\frac{\sigma_c}{\alpha}\right)^2 = 0 \tag{28}$$

This equilibrium criterion marks an unstable fixed point, in that any value of σ_c/α above a critical value will cause nett contraction of the islands ($\Delta\mu_i<0$), which in turn decreases α and farther removes the grain boundary from the equilibrium point. Similarly, once σ_c/α falls below a critical value determined by equation (5) (i.e., $\Delta\mu_i>0$), island growth causes σ_c/α to decrease further, continuing to remove the grain boundary farther from equilibrium. Initially, α will likely be small (of the order of a few percent; van Noort et al., 2008), so that the onset of static island growth can only be reached by lowering σ_c by porosity reduction (compaction). It is therefore expected that there exists a critical aggregate porosity below which island growth initiates (van Noort et al., 2008).

Equation (25) is an ill-conditioned equation containing two unknowns, V_{ps} and $\dot{\alpha}$, and cannot be solved analytically without further constraints linking V_{ps} and $\dot{\alpha}$, beyond the end-member cases represented by equations (26) and (27). In the absence of such constraints, and noting the numerous simplifications and approximations made in deriving equation (25) for V_{ps} and $\dot{\alpha}$, a first-order solution to acquiring V_{ps} and $\dot{\alpha}$ can be obtained by assuming that at any instant the pressure solution process and the tendency for islands to increase in area operate independently. In line with this, we take the rate of pressure solution at an evolving grain contact to be given by equation (26) at any instant, with α evolving with time according to equation (27).

3.2. Grain Boundary Connectivity

It was mentioned in section 2 that the connectivity and diffusive properties of a grain boundary depend on the structure of the grain contact. The evolution of the grain boundary as described by the above model formulations must therefore be reflected by the transport properties of the grain boundary, which we will detail below.

Several microstructural studies have shown that healed grain boundaries contain arrays of fluid inclusions in the form of isolated spheres or tubes (e.g., Desbois et al., 2012; Hickman & Evans, 1991; Urai et al., 1986). In grain boundaries that show a lesser degree of healing, these tubes connect up with neighboring inclusions to form a network that connect the interior of the grain boundary to the pore space (Ghoussoub & Leroy, 2001; Spiers & Schutjens, 1990). If the density of inclusions, tubes, and pits is high enough, they can provide an interconnected pathway from the center of the grain boundary into the pore space. In general, this will apply to a statically healing grain boundary and also to a dynamically wetted grain boundary island-channel structure undergoing progressive structural evolution during pressure solution. To estimate the probability that a given location within the grain boundary is connected to the pore space and to quantify how the transport properties of the grain boundary change with asperity size and area fraction, we employ percolation theory, following standard percolation theory formulations (see Stauffer & Aharony, 1992).

In this framework, any random location in the grain boundary rim is assigned an "open" or "closed" state. In our current view of a grain boundary, the open state corresponds to a channel and is open to the diffusive mass flux. The closed state can be seen as an asperity (solid-solid) contact. The probability p of a site being open is related to the relative asperity contact area α as follows:

$$p = \frac{A_{sl}}{A_c} = \frac{A_c(1-\alpha)}{A_c} = 1-\alpha \tag{29}$$

The probability of a site being closed is then $(1-p) = \alpha$. It can be shown that in an infinitely large system, clusters of open sites that traverse the entire length of the system exist (i.e., percolation occurs) only when $p>p_c$. The value of p_c can be calculated (analytically or numerically) for various geometries or, in the current situation, can be estimated from microstructural estimates of α in the fully sealed state (so that $p_c=1-\alpha_c$), assuming that mass and fluid transport do not proceed once a contact has fully healed (with the term "healing" loosely referring to the progression of asperity growth; cf. van Noort et al., 2008). Furthermore, numerous universal scaling relations have been derived that describe transport properties of the system. For instance, the effective diffusivity of a system of infinite size can be expressed as follows:

$$D^{\text{eff}} \propto (p - p_c)^{\nu} \tag{30}$$

Here, ν assumes a value of 1.16 in 2-D (Sahimi, 2003). To determine the proportionality constant, we assume that in the initial, unhealed state, $\alpha = \alpha_0$, $p = p_0 = 1 - \alpha_0$, and $D^{\text{eff}} = D^0$, so that (30) becomes:

$$D = D^{\text{eff}} = D^0 \left(\frac{[p - p_c]}{[p_0 - p_c]} \right)^{\nu} = D^0 \left(\frac{\alpha_c - \alpha}{\alpha_c - \alpha_0} \right)^{\nu} \tag{31}$$

Note that we implicitly assume that the system is infinite in size, which is a valid approximation when the sizeof the grain-grain contact far exceeds the characteristic size of an open site (etch pit, fluid inclusion, or tube size). In the case where this assumption is not valid, the percolation threshold p_c is expected to decrease in magnitude, and percolation of the system is more likely. Additional scaling can be performed to better represent percolating clusters of finite size (see Stauffer & Aharony, 1992).

As the asperities increase in size, α increases toward α_c, and p approaches p_c. For $p \leq p_c$ (and equivalently $\alpha \geq \alpha_c$), no percolation occurs and the grain boundary is said to be fully healed and sealed, effectively terminating pressure solution. Mass transfer may still occur internally to restructure the island-channel network, breaking up the network in tubes and isolated fluid inclusions (Brantley, 1992). During this, the proportion of fluid stored in the grain boundary is thought to remain unchanged. Based on microstructural accounts of healed grain boundaries (see, e.g., Desbois et al., 2012; Ghoussoub & Leroy, 2001; Schutjens, 1991; Urai et al., 1986), we estimate that the grain contact surface area occupied by solid falls between 0.5 and 0.8, which bounds the range of values for α_c. The value of p_0 is estimated to exceed 0.9, corresponding to $\alpha_0 < 0.1$, as suggested by Renard et al. (2012) and van Noort et al. (2008), although it can be argued that near the onset of progressive grain boundary island growth, α attains higher values (van Noort et al., 2008). Taking then values of p_0, p_c, α_0, and α_c, and using equation (27) to describe $\dot{\alpha}$, equation (31) now provides a description of the evolution of D^{eff}.

It is evident how a moderation of the transport properties of the grain boundary can result in a reduction of the rate of pressure solution, if it is limited by the rate of diffusion (like for halite at room temperature). In the case that the rate of pressure solution is controlled by the interface reaction rate (like for quartz in the experiments of Niemeijer et al., 2002), the influence of an evolving grain boundary structure will only manifest itself in the overall pressure solution rate when D^{eff} has been reduced sufficiently for the process to become controlled by the rate of diffusion. In other words, a switch in rate-limiting process is anticipated in materials for which pressure solution is initially interface reaction controlled.

3.3. Scale Dependence of Grain Boundary Topography

Throughout this section, it has been assumed that the average grain boundary roughness S is time and scale invariant. However, it cannot be excluded that this roughness is dependent on the size of the contact or on grain boundary stress (cf. Schutjens & Spiers, 1999). We will explore this possibility in more detail by considering a scale dependence of S.

It has been suggested in numerous studies that (dynamic) interfaces are self-affine, including natural faults and joints (Brown & Scholz, 1985; Brodsky et al., 2016; Candela et al., 2012), stylolites (Gratier et al., 2005; Renard et al., 2004), processed or naturally corroded metal surfaces (Majumdar & Tien, 1990; Shanhua et al., 2015; Zahouani et al., 1998), and various geomaterials (Avnir et al., 1984; Dieterich & Kilgore, 1996; Wong et al., 1986). Owing to its self-affine character, a given surface will appear smoother at larger length scales. When it is assumed that the average thickness of a grain boundary is controlled by its roughness, then self-affinity implies that $S \propto L^H$, where L is a characteristic length scale (i.e., the size of the contact) and H is the Hurst exponent (with $H \neq 1$ for self-affine surfaces; Brodsky et al., 2016). A dynamically evolving grain boundary may not obey such a scaling law, as the topography may be strongly controlled by fluid-rock interactions. However, a size-dependent topography is well established for stylolites over 4–5 orders of magnitude (see Gratier et al., 2013, and references therein) and has previously been reported for grain interfaces undergoing pressure solution at the micrometer scale (de Meer et al., 2002, 2005; Schutjens & Spiers, 1999). De Meer et al. (2005) report that the average grain boundary thickness increases with increasing contact width. This can also be inferred from the observed increase in kinetic constant DCS with increasing contact width (de Meer et al., 2002), assuming that D and C are scale independent. Furthermore, Schutjens and Spiers

(1999) observed contact roughness at all resolvable scales, ranging from tens of micrometers to a few hundreds of nanometers, suggesting a fractal topography. Finally, stressed interfaces deforming by elastic and/or plastic yield are well characterized by a fractal relationship (Brown & Scholz, 1985; Dieterich & Kilgore, 1996).

Since the chemical potential for asperity growth (or undercutting) depends strongly on S (see equation (27)), the possibility that S scales with contact size needs to be considered. Therefore, we define S to vary with r_c, following a power law scaling relationship, in line with our preceding discussion of such effects. More specifically,

$$S = S^{\mathrm{ref}}\left(\frac{r_c}{r_c^{\mathrm{ref}}}\right)^H \tag{32}$$

Here, S^{ref} is a reference value corresponding to a radius of contact r_c^{ref}, and H is the Hurst exponent. A value of H=0 results in a scale-independent (constant) value of S. Using this relation, the asperity growth rate as predicted by equation (27)is altered through the surface energy term, which contains S in the denominator.For consistency, the value of S as appearing in the experimentally determined product DCS in equation (1) is also scaled using the above relation, so that both the rate of pressure solution and that of asperity growth are affected by the simulated changes in topography. When scaling DCS, we assume that the experimentally determined value of this product corresponds to DCS^{ref}, so that the product scales as $DCS^{\mathrm{ref}}\left(r_c/r_c^{\mathrm{ref}}\right)^H$. Note that equation (32) is purely empirical in nature and therefore has little predictive power. However, we will only use this relationship to investigate the possible effects of a scale-dependent contact roughness on the grain boundary island growth behavior, by comparing simulations with constant S to those where S is scaled.

3.4. Analytical Model for Pressure Solution With Grain Boundary Evolution

Classically, the constitutive relations for pressure solution creep are derived for a single contact, before being upscaled to the size of the (porous) aggregate, assuming an average unit cell geometry and stress distribution (see, e.g., Pluymakers & Spiers, 2015; Rutter & Elliott, 1976; Spiers & Schutjens, 1990). For obtaining a description of pressure solution with grain boundary evolution analytically, we adopt classical treatments of the model aggregate by assuming a well-defined relationship between bulk porosity and the area (or equivalent radius) of an individual grain-grain contact. This relationship reads (Pluymakers & Spiers, 2015):

$$r_c = d\sqrt{\frac{F}{\pi Z}f(\phi)} \tag{33}$$

Here, F is a shape factor that assumes a value of π for spherical grains and Z is the bulk average coordination number (modulated by $f(\phi)$). $f(\phi)$ is a smooth function that describes the evolution of contact area and coordination with porosity and is chosen such that $f(\phi_0)$=0 and $f(0)$=1. Compare Spiers et al. (2004), we define $f(\phi)$ as follows:

$$f(\phi) = \frac{\phi_0 - \phi}{\phi_0} \tag{34}$$

In this expression, ϕ_0 corresponds to the porosity at the start of the experiment, where the area of contact of grains is relatively small. Using relation (33), the constitutive equations (26) and (27) can then be upscaled from a single grain-grain contact to an assembly of packed grains to give:

$$\dot{\varepsilon} = 4\pi A_\varepsilon\left(\frac{Z}{F}\right)^2\frac{DCS(1-\alpha)\Omega}{RT}\frac{\sigma_e}{d^3 f(\phi)^2} \tag{35a}$$

$$\frac{\mathrm{d}\phi}{\mathrm{d}t} = -(1-\phi)\,\dot{\varepsilon} \tag{35b}$$

$$\frac{\mathrm{d}\alpha}{\mathrm{d}t} = 8\pi\frac{Z}{F}\frac{DC(1-\alpha)\Omega}{RTd^2 f(\phi)}\left(\frac{2\gamma_{\mathrm{sl}}}{S}\Delta\cos\frac{\theta}{2} + \frac{1}{2E}\left[\frac{Z}{F}\frac{\sigma_e}{\alpha f(\phi)}\right]^2\right) \tag{35c}$$

Here, A_ε is a geometric factor that assumes a value of 6 for isotropic compaction (Pluymakers & Spiers, 2015). D is modified by α through equation (31) and S through equation (32). The full set of coupled differential

equations (equation (35)), complemented with equations (31) and (32), is solved iteratively using the *SciPy* ODE package (Jones et al., 2001) to yield the evolution of D, α, strain rate, strain, and porosity with time.

In this presented form, equation (35) encompasses numerous kinetic, geometric, and structural parameters, each involving various degrees of uncertainty. However, in accordance with the Buckingham π theorem, the number of truly independent parameters that govern the system's dynamics can be reduced greatly by making the following nondimensional substitutions:

$$t' = t\frac{DC\Omega\sigma_e}{RTd^2} \tag{36a}$$

$$S' = \frac{S}{d} \tag{36b}$$

$$\Gamma_{\mathrm{sl}} = \frac{2\gamma_{\mathrm{sl}}}{d\sigma_e}\Delta\cos\frac{\theta}{2} \tag{36c}$$

$$\Gamma_{\mathrm{el}} = \frac{\sigma_e}{2E} \tag{36d}$$

$$G = \frac{Z}{F} \tag{36e}$$

which gives

$$\frac{\mathrm{d}\phi}{\mathrm{d}t'} = -(1-\phi)4\pi(1-\alpha)A_\varepsilon S'\left[\frac{G}{f(\phi)}\right]^2 \tag{37a}$$

$$\frac{\mathrm{d}\alpha}{\mathrm{d}t'} = 8\pi(1-\alpha)\left[\frac{G}{f(\phi)}\right]\left(\frac{\Gamma_{\mathrm{sl}}}{S'} + \left[\frac{G}{f(\phi)}\right]^2\frac{\Gamma_{\mathrm{el}}}{\alpha^2}\right) \tag{37b}$$

Since the parameters A_ε and G are constrained by geometry, the only parameters governing the dynamics of α and ϕ that involve experimental uncertainty are S', Γ_{sl}, and Γ_{el}. Out of these three parameters, only S' can be said to be poorly constrained by laboratory measurements. In the case that scaling of D and S is accounted for, two additional parameters (α_c and H) appear that are not fully constrained (α_0 is constrained by the initial condition of α, and ν is fixed to a value of 1.16 in 2-D; Sahimi, 2003). The sensitivity of the model outcomes to S' and H will be investigated in more detail in section 4.2 and discussed further in section 5.1. For the convenience of comparison with laboratory parameters and values, all quantities and equations will be used in their dimensional form throughout the remainder of this work.

Lastly, even though this upscaling strategy is highly simplistic, it has been shown to yield valid results in the case of uniaxial compaction of granular aggregates (Pluymakers & Spiers, 2015; Rutter & Elliott, 1976; Spiers & Schutjens, 1990). Furthermore, when other deformation mechanisms operating contemporaneous with pressure solution creep are to be considered (such as grain microcracking), their respective contributions to the overall strain rate are additive, so that equation (35a) can be extended as a sum over the strain rates of the individual mechanisms. The total strain rate then enters equation (35b) to describe the rate of change of porosity, which in turn feeds back into $f(\phi)$—see, for example, Chen and Spiers (2016).

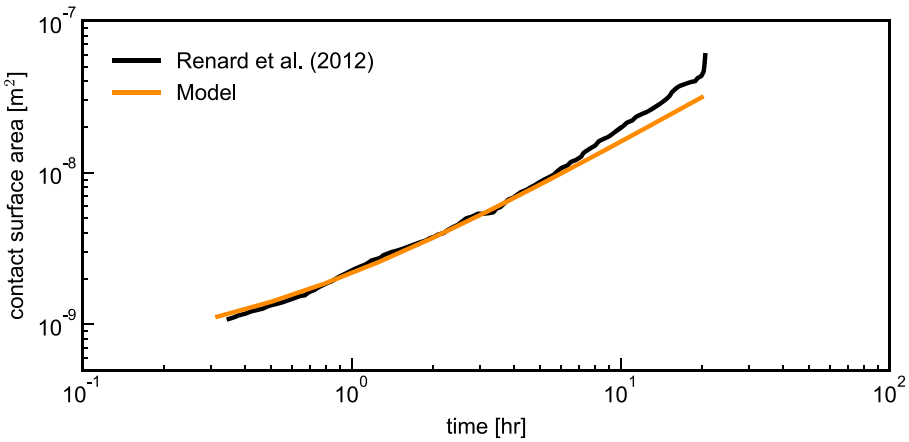

Figure 2. Comparison of the model-predicted evolution of asperity growth (equation (38)) with the experimental observations of Renard et al. (2012; data taken from their Figure 9b).

4. Analytical Model Predictions Versus Experiments on Halite

4.1. Single-Contact Compression

As a first test of the model derived in the present study, we compare predictions of the increase of solid-solid contact area with experimental observations of contact asperity growth reported by Renard et al. (2012). In these experiments, a transparent halite plate was pressed against a glass base plate, and the evolution of the area of contact between the halite and the glass plates ("asperities" in the terminology of Renard et al., 2012) was monitored with an optical microscope connected to a camera. After introduction of a reactive pore fluid (brine), individual asperities were observed to increase in size, even though the change in distance between the two plates was measured to be negligibly small. The absence of convergence indicates that pressure solution or other deformation processes were absent, which matches the end-member scenario assumed by equation (27).

For an initial value of α=0.01 and applied stress of σ_e=0.26 MPa, the average elastic strain energy stored in the asperities is approximately 9 kJ/m^3, which is of the same order as the surface energy term in the onset criterion given by equation (5) (substituting γ_{sl}=0.2 J/m^2, $\Delta\cos\frac{\theta}{2} = 0.18$, and S=8.6μm as estimated by Renard et al., 2012). From the onset of asperity growth the elastic strain energy contribution to the dynamics of asperity growth decreases quadratically with increasing α and so rapidly becomes negligible compared to the surface energy contribution. When the elastic strain energy contribution to equation (27)is neglected, the resulting ordinary differential equation can be solved analytically to give:

$$\alpha(t) = 1-(1-\alpha_0)\exp\left(-t\frac{16DC\Omega}{RTr_c^2}\frac{\gamma_{sl}}{S}\Delta\cos\frac{\theta}{2}\right) \tag{38}$$

where t is the time since the onset of asperity growth. For small values of the argument of the exponential, α increases approximately linearly with time (since $\exp(x)\approx 1+x$ for $x\to 0$), in agreement with the observations of Renard et al. (2012).

Substituting values of D=2×10^{-9} m^2/s, C=0.15 m^3/m^3, T=295 K, r_c=0.56 cm, and S=8.6 μm (all taken from Renard et al., 2012) and additionally γ_{sl} and $\Delta\cos\frac{\theta}{2}$ as cited above, we obtain a well-constrained evolution of asperity growth with time. Comparison of the evolution predicted by equation (38)with experimental observations shows excellent agreement (Figure 2). This agreement suggests that the contact-scale model given by equation (27) can quantitatively capture the dynamics of contact asperity growth.

4.2. Granular Aggregate Compaction

After having tested the present model at the contact scale in the absence of pressure solution, we now continue to test the model performance when pressure solution operates. Here, we compare the deformation rates measured by Schutjens (1991) in long-term compaction experiments with the results of our extended

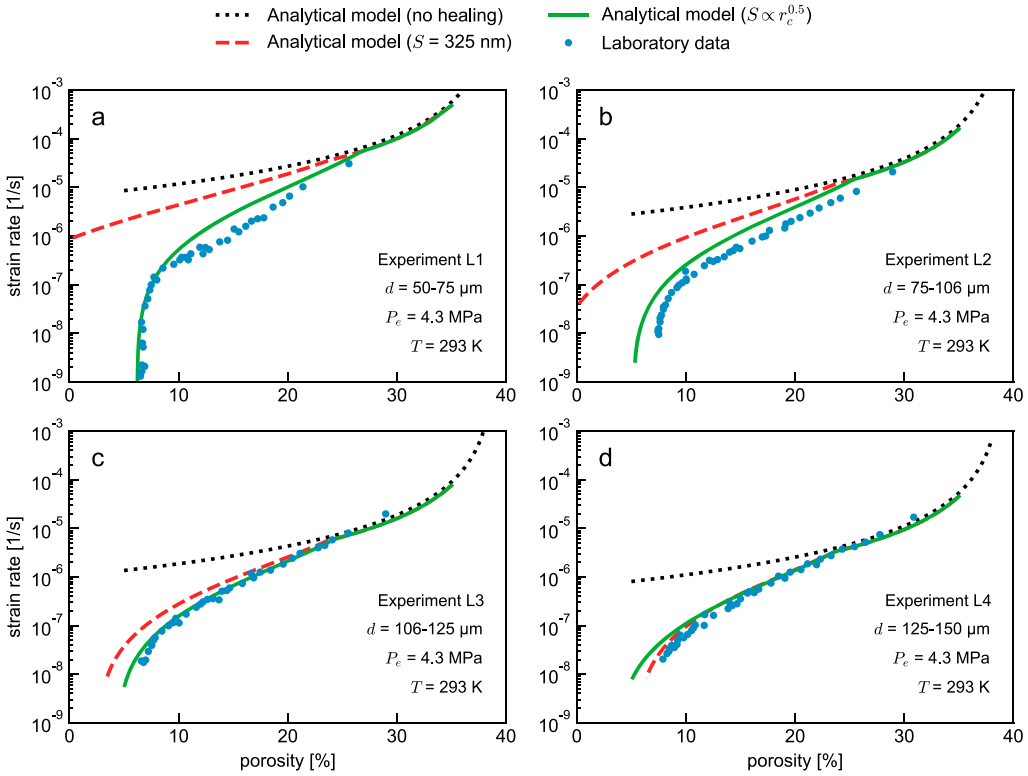

Figure 3. (a–d) Comparison between analytical models and the laboratory results of Schutjens (1991). For each laboratory data set, three model results are shown: one where no grain boundary evolution is considered (i.e., equation (35) with $\dot{\alpha} = 0$), one where grain boundary evolution is considered with a constant value of S=325 nm, and one where grain boundary evolution is considered with $S \propto r_c^H$ and H=0.5. Experimental parameters are as indicated in each panel.

model for pressure solution plus grain boundary evolution as expressed by equation (35). For this comparison, we require laboratory data from high-strain (ϕ<20%) compaction tests performed under conditions for which diffusion-controlled pressure solution is the dominant deformation mechanism, limiting the contribution of, for example, microcracking to the overall rate of compaction. Moreover, the kinetics of pressure solution need to be well constrained, so that uncertainties in the model constitutive parameters can be excluded to contribute to discrepancies between the laboratory data and model predictions. To our best knowledge, only the data set reported by Schutjens (1991) satisfies these specific criteria, and so we will compare our model outcomes to this data set. The details of the experimental procedure are given in Appendix .

We start by comparing the predictions of grain boundary evolution (equation (35)) for a constant value of S with the laboratory data of Schutjens (1991). This comparison is made for each experiment individually—see Figure 3. The parameters used in the analytical models are given in Table 1. First, we examine a model that does not consider grain boundary evolution, that is, using equation (35) with $\dot{\alpha} = 0$, so that α and D are constant. At high porosities, there is acceptable agreement between the strain rates predicted by the model and measured in the experiments, but for porosities <25% the analytical model starts to overestimate the compaction rates. Near the terminal porosity of the experiments, the mismatch between model and experimental strain rates is up to several orders of magnitude, illustrating that the existing theory of pressure solution does not describe the compaction behavior at porosities below 20%.

Next, we consider a model where the grain boundary structure evolves, with $\dot{\alpha}$ being described by equation (35c) and D being modified by the instantaneous value of α in accordance with equation (31). The comparison between the experimental data and model predictions including grain boundary evolution (Figure 3) shows that when a constant value of S=325 nm is taken, only the data for a grain size range of 125–150μm (Figure 3d) can be accurately represented by the model, while for all other grain size ranges (Figures 3a–3c), the model overestimates experimental compaction rates and underestimates the terminal porosity. Although

Table 1
Parameters Used in the Analytical Model Simulations

Parameter	Value	Units
Nominal grain diameter	62.5, 90.5, 115.5, 137.5	μm
Effective pressure (P_e)	4.3	MPa
Initial porosity (ϕ_0)	40.0	%
Geometric constant (A_ε)	6	—
Grain shape factor (F)	π	—
Grain coordination number (Z)	6	—
Kinetic constant (DCS)	1.22×10^{19}[a]	m^3/s
Molar volume (Ω)	2.69×10^{-5}	m^3/mol^3
Temperature (T)	294	K
Surface energy (γ_{sl})	0.2[b]	J/m^2
Dihedral angle mismatch ($\Delta\cos\frac{\theta}{2}$)	0.18[c]	—
Asperity Young's modulus (E)	37	GPa
Initial asperity occupation ratio (α_0)	0.15	—
Terminal asperity occupation ratio (α_c)	0.8	—
Reference grain boundary thickness (S^{ref})	325	nm
Reference contact radius (r_c^{ref})	35	μm
Hurst exponent (H)	0.5	—

*Note.*The sequence of grain sizes above corresponds to the mean of the grain size ranges of experiments L1, L2, L3, and L4, respectively, as reported by Schutjens (1991). [a]Spiers et al. (1990). [b]Visser (1999) using the approximation by Israelachvili (1986). [c]Lewis and Holness (1996).

the model with constant S broadly displays the same features as the experimental data, the fit between the analytical models and compaction data is much improved by allowing S to evolve with the size of the grain contact (equation (32)), suggesting a scale dependence of S as discussed in section 3.3. However, it should be noted that in the analytical model approach, upscaling from the grain contact scale to that of the aggregate (i.e., relating mean grain contact size to porosity) involves an empirical porosity function $f(\phi)$. While this has been shown to be accurate for a wide porosity range (Niemeijer et al., 2002; van den Ende et al., 2018; Zhang et al., 2010), it cannot be excluded that the apparent scale dependence of S stems from the functional form of $f(\phi)$, which may not accurately represent the evolution of grain contact area and coordination number with porosity in the experimental samples at lower porosities. Additionally, the polydispersed (multivalued) distribution of grain sizes in the laboratory aggregates, as well as the presumed circular contact geometry, may affect the apparent scale dependence of S.

Finally, we compare two models that consider a scale dependence of $S \propto r_c^H$, with Hurst exponents H=0.5 and H=1.1 as suggested by roughness measurements of natural stylolites (e.g., Renard et al., 2004)—see Figure 4. From the comparison, it is evident that the overall compaction rates are sensitive to the value of H and that the laboratory data can only be explained by a model with a Hurst exponent of 0.5.

5. Discussion

The analytical model has been compared with laboratory data for isostatic compaction of NaCl aggregates, as reported by Schutjens (1991). The comparison shows good agreement regarding the trends in compaction rates, demonstrating that grain boundary evolution involving an increase in solid-solid contact area associated with a decrease in surface energy can explain the retardation of pressure solution creep rates. In spite of the good quantitative match between the laboratory data and the models, a number of issues remain unresolved. Most notably, the structure and dynamics of a wetted grain boundary, and its relation to pressure solution, require further discussion. In addition, the relevance and implications of the present findings for pressure solution in nature require examination. These topic will be addressed in the following sections.

5.1. Structure and Dynamics of a Wetted Grain Contact Under Stress

In classical analytical treatments of steady-state pressure solution (e.g., Lehner, 1995; Pluymakers & Spiers, 2015; Spiers & Schutjens, 1990), the smallest scale that is explicitly considered encompasses a segment of a grain contact over which a representative average grain boundary structure can be assumed. The local dynamics of grain contact structure is not made explicit in these models. Instead, a fixed, steady-state

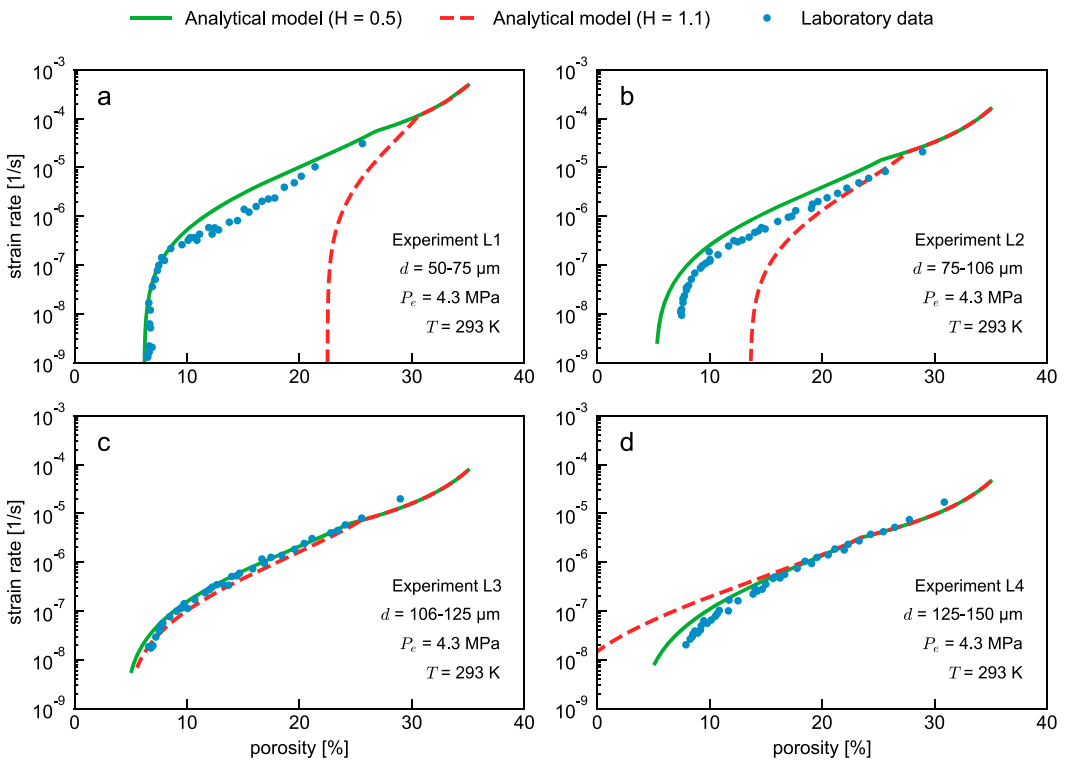

Figure 4. (a–d) Comparison between analytical models and the laboratory results of Schutjens (1991). For each laboratory data set, two model results are shown: one where grain boundary evolution is considered with $S \propto r_c^H$ and H=0.5 (solid line) and one with H=1.1 (dashed line). Experimental parameters are as indicated in each panel.

structure is assumed. However, for a rigorous investigation of the evolution of the structure of a wetted grain boundary under stress, this local scale needs to be considered explicitly, without assuming steady state. In our analysis presented in section 3.1, we made a number of simplifying assumptions regarding the distribution of the local free energy and the structure of the grain boundary zone. These assumptions were required in order to derive closed-form expressions for the structural evolution of the grain boundary, given our present knowledge on the processes that control the dynamics of dissolution, diffusion, and precipitation at the scale of a single island.

An important gap in our knowledge remains the lack of a quantitative description of the processes that cause the grain boundary to remain dynamically rough when subjected to a sufficiently high state of stress. See-through experiments (Schutjens & Spiers, 1999) demonstrate that an optically flat interface undergoing pressure solution can regenerate a rough topography when the stress supported by the interface is raised. Such behavior is not reflected by our present model describing grain boundary evolution (equation (27)). Closely related to these observations is the possibility that the grain boundary roughness and correspondingly the mean thickness S of the interstitial fluid film are scale dependent. In situ spectroscopy experiments performed by de Meer et al. (2005) on a single grain contact revealed that S increases over time, concurrent with widening of the stressed interface. However, it is presently not clear whether this is a transient effect or if a steady-state value of S is attained for a constant size of the contact.

In the context of the topographic evolution of stylolites, Renard et al. (2004; see also Schmittbuhl et al., 2004) proposed a Langevin-type model describing the growth of stylolites as a competition between stress-induced roughening and surface energy-driven smoothening, in the presence of stochastic noise (e.g., spatiotemporal heterogeneity in dissolution kinetics). This model predicts an effective Hurst exponent of H=1.2 at small length scales, and H=0.4 at large length scales, corresponding with the dominance of either stress or surface energy in controlling the dynamics of the system, respectively. The transition from one regime to the other is governed by a characteristic length scale l_c, given as follows:

$$l_c = \frac{E\gamma_{sl}}{2\sigma_0^2(1-\nu^2)} \tag{39}$$

where σ_0 is the normal stress acting across the stylolite dissolution plane and ν is the Poisson ratio of the solid. The predicted values of the Hurst exponent and the interpretation of l_c were found to be in good agreement with measurements of the Hurst exponent for natural stylolite samples, which were characterized by end-member Hurst exponents of H=0.5 and H=1.1. By interpreting a stressed grain contact undergoing pressure solution as a "microstylolite," the corresponding value of the Hurst exponent (either 0.5 or 1.1) can be estimated based on the magnitude of l_c relative to the size of the grain contact. For porosities larger than zero, the stress acting across the contact is amplified with respect to the externally imposed stress or effective pressure (4.3 MPa in the experiments of Schutjens, 1991), and so we adopt an elevated contact stress value of σ_0=σ_c=20 MPa. Further substitution of E=37 GPa, γ_{sl}=0.2 J/m^3, and ν=0.25 yields a characteristic length scale l_c=10 μm, which is smaller than the mean grain contact size (being of the order of the grain size). This estimation suggests that on the scale of the grain contacts, long-range stress effects dominate the dynamics and accordingly the Hurst exponent assumes a value of 0.4–0.5, in agreement with the estimated value of H=0.5 in the simulations.

Following the reasoning above, it can be argued that materials other than halite (e.g., calcite) will exhibit similar values of l_c at a given value of stress, as l_c is only linearly dependent on the material/interface properties (E, γ_{sl}). On the other hand, the effective contact stress exerts a quadratic control on l_c, and so the model of Renard et al. (2004) predicts a strong sensitivity of the grain contact Hurst exponent on porosity, fluid pressure, and applied stress. Furthermore, for aggregates exhibiting small grain sizes of the order of micrometers (such as for fault gouges), the grain contact size will generally be much smaller than l_c, so that compaction of such aggregates is expected to be governed by a Hurst exponent in the range of 1.1–1.2. As can be seen in Figure 4a, such an increase in Hurst exponent dramatically diminishes the rate of compaction by pressure solution for small grain sizes. Laboratory measurements of compaction of coarse-grained aggregates may therefore not be representative for those of fine-grained aggregates.

5.2. Relation Between Grain Boundary Evolution and Intergranular Pressure Solution

When considering static island growth driven by surface energy (e.g., van Noort et al., 2008), each individual island may have an unconstrained (infinite) lifetime, in that it may grow without being completely removed by dissolution over the lifetime of the grain contact. However, in order to achieve grain convergence when pressure solution operates, it is required that the entire grain boundary zone fully dissolves and rejuvenates its islands in a finite amount of time. If this were not the case, that is, if islands would not fully dissolve, then nett dissolution would only occur by deepening of the channels (increasing S), which does not produce grain convergence. As a corollary, the lifetime of each individual island must be finite (i.e., it must fully dissolve), and new islands must form by nonuniform dissolution and compression of the grain contact, if pressure solution were to operate. This provokes a paradoxical interpretation of the grain boundary evolution model described in section 3: An increasing value of α (the area fraction occupied by islands) seems suggestive of growth of individual islands, similar to the case of static island growth with no pressure solution. However, α reflects a spatial average of the total area occupied by islands, rather than describing the size and shape of individual islands. During active pressure solution, the nett rate of dissolution of islands may be reduced (induced by local changes in free energy) compared to the rate of formation of islands, resulting in a nett increase in α, even though islands still exhibit a finite lifetime.

Although it is explicitly assumed in the model derivation of section 3.1 that pressure solution is operative during (dynamic) grain boundary evolution, it can be questioned whether this assumption is valid or whether pressure solution is immediately arrested as soon as the nett volume occupied by islands starts to increase (static growth). A number of optical imaging experiments report negligible convergence during growth of interface asperities (Renard et al., 2012) or of the stressed contact between a plano-convex lens pressed against a flat plate (Beeler & Hickman, 2015; Hickman & Evans, 1991, 1992), under conditions favorable for pressure solution. These observations suggest that pressure solution does not operate during structural evolution of the grain contact. However, as was noted by Schutjens and Spiers (1999), the plano-convex geometry employed in the experiments of Hickman and Evans (1991, 1992; and of Beeler & Hickman, 2015) promotes contact growth due to the large radius of curvature at the contact margin. In the experiments of Renard et al. (2012), the nominal contact stress was low (0.26 MPa) and the contact asperities large in size (up to

300 μm). These experiments may therefore not be representative for our envisioned dynamic island-channel structure at the scale of tens to a few hundreds of nanometers.

In optically monitored grain-to-grain contact experiments conducted by Schutjens and Spiers (1999), all experiments showed convergence concurrent with an evolving grain boundary structure. Particularly, their experiment T4 displayed a gradual smoothing of an initially rough grain contact over the course of 25 days, until an optically smooth interface topography was achieved. Upon stepwise increasing the load on the contact, the grain contact reroughened and the initial roughness was recovered (see Figure 10 in Schutjens & Spiers, 1999). This example illustrates that pressure solution can continue to operate during grain boundary evolution.

5.3. Implications of the Present Findings for Pressure Solution in Nature

We have established that grain boundary evolution may significantly retard pressure solution creep rates in monomineralic aggregates at high volumetric strains and low porosities (<20%). Our models for pressure solution concurrent with grain boundary evolution have been compared with isostatic compaction data on halite, which has previously been adopted in laboratory tests as an analog material for quartz at hydrothermal conditions (Bos et al., 2000; Niemeijer et al., 2009). Although the material properties of halite are dissimilar from those of quartz, the processes involved in deformation of halite aggregates (e.g., pressure solution) have similarly been recognized to operate in quartz aggregates at the relevant conditions (de Boer et al., 1977; Heald, 1955; van Noort et al., 2008). This notion receives further support from the high-strain compaction tests performed on quartz by Niemeijer et al. (2002), reporting similar compaction trends at temperatures in the range of 400–600 °C as have been observed by Schutjens and Spiers (1999) in halite at room temperature conditions. Even though the process that limits the rate of pressure solution at high porosities is different for halite at room conditions than it is for quartz at hydrothermal conditions (diffusion versus dissolution, respectively; Niemeijer et al., 2002; Schutjens & Spiers, 1999), it is expected that diffusion will become rate limiting for both materials at low porosities (see section 3.2). The models for pressure solution and grain boundary evolution derived in this study may therefore generally apply to other materials, in a laboratory setting as well as in nature.

In contrast to many laboratory tests performed on monomineralic aggregates, natural sediments and fault gouges are often heterogeneous in composition. Given that solid-liquid and solid-solid interface energies play an important role in controlling the structural evolution of grain boundaries, the efficiency of grain boundary evolution as envisioned in this work can be challenged. A reduced efficiency of grain boundary evolution driven by surface energy has been observed in several laboratory experiments: Beeler and Hickman (2015) observed that quartz-sapphire interfaces of compressed plano-convex lenses do not show grain contact spreading (neck growth), in contrast to quartz-quartz interfaces. Similarly, the inhibiting effect of bimineral interfaces was inferred from the difference in convergence rates measured in experiments conducted on halite-halite and halite-silica interfaces (Hickman & Evans, 1991). Hickman and Evans (1992) showed that neck growth is faster for monomineralic interfaces with a lower crystallographic misorientation. And lastly, in the compaction experiments of Zubtsov et al. (2004), pure halite aggregates displayed lower compaction rates than mixtures of halite and calcite, even though calcite is characterized by slower pressure solution kinetics than halite. This behavior was attributed to a reduced efficiency of healing of halite-calcite interfaces and correspondingly the inhibition of retardation of pressure solution as compared to pure aggregates. These observations suggest that the potential for grain boundary evolution is reduced by the solid-liquid and solid-solid interfacial energies associated with an incompatible bimineral configuration or possibly by a strong contrast in dissolution or precipitation rates of each of the minerals in contact. This has implications for the compaction behavior of polymineralic aggregates in nature: Relatively pure (monophase) aggregates may experience significant retardation in pressure solution creep rates at low porosities, whereas mixed, polyphase aggregates may not. This effect is noticeable when comparing compaction rates of single-phase aggregates with polyphase aggregates in laboratory compaction tests (e.g., Niemeijer & Spiers, 2002; Zubtsov et al., 2004).

The operation (or absence) of grain boundary evolution holds important implications for the time-dependent restrengthening of faults. It is generally acknowledged that (in the presence of a reactive pore fluid) natural faults densify during interseismic times, for which pressure solution creep is an important mechanism at in situ conditions (Chester & Chester, 1998; Evans & Chester, 1995; Holdsworth et al., 2011; Smeraglia et al.,

2017). The compaction of faults is thought to contribute to the restrengthening of a fault after a seismic event (Angevine et al., 1982; Sleep & Blanpied, 1992; Yasuhara et al., 2005), and so faster compaction rates would result in a larger buildup of frictional strength over a seismic cycle. If grain boundary evolution operates efficiently, compaction and frictional restrengthening by pressure solution may be severely inhibited. On the other hand, it was remarked by Hickman and Evans (1991) that healed interfaces exhibit significant cohesive strength, and so grain boundary evolution (and associated sealing of the grain boundary) may contribute to the total fault strength by generating contact-scale cohesion. The time-dependent strengthening of fault could therefore arise from compaction by pressure solution and from cohesion generated by grain boundary evolution (as was recently observed by van den Ende & Niemeijer, 2019). Naturally, fault strengthening through grain contact sealing requires that the structure of the grain boundaries be unperturbed by contact renewal processes such as granular flow, contributing to the competition between time-dependent strengthening and slip-dependent weakening (e.g., Chen & Spiers, 2016). In fault gouges of polymineralic composition (particularly when phyllosilicates are abundant) restrengthening by compaction is promoted, but restrengthening by time-dependent cohesion may be negligible if grain boundary island growth is the sole mechanism for generating cohesion. This presents opportunities for future research and an application of the models developed in this work in the context of fault and earthquake mechanics.

6. Conclusions

In this study, we have derived expressions that describe the evolution of the grain boundary structure within stressed grain contacts undergoing pressure solution. We have focused on the interplay between growth in asperity contact area and pressure solution creep and the ultimate cessation of pressure solution when the grain boundary fluid connectivity breaks down, in the approach to the percolation threshold. The resulting analytical relations describing the rate of pressure solution and of the increase in grain boundary solid contact area at individual grain contacts have been used to predict single contact and aggregate behavior, assuming a uniform pack of identical grains to upscale contact behavior to the aggregate scale. The predicted rate of growth of contact-scale asperities has been directly compared with optical measurements of Renard et al. (2012) on halite-glass single interfaces. The upscaled compaction behavior of granular aggregates as predicted by our new model has been compared with the compaction experiments on NaCl conducted by Schutjens (1991). From these comparisons, we conclude the following:

1. Overall, grain boundary evolution involving asperity growth can explain the large reduction in pressure solution strain rates with decreasing porosity seen in experiments. The discrepancy between experimental compaction rates and predictions from analytical models that do not include grain boundary evolution (i.e., when the grain boundary structure and effective diffusivity are constant) can be fully accounted for when an evolving grain boundary structure and fluid channel constriction are considered.
2. When a constant value for the grain boundary thickness (S) is assumed, the predicted strain rates do not compare well with the full laboratory data set. Rather, model results with constant S only compare well for a single specific grain size range, suggesting that the grain size dependence is not captured properly. However, when S is assumed to scale with the size of the contact, corresponding to a self-affine grain boundary topography, the entire data set can be modeled with a single set of parameters. While this does not prove that S is scale dependent, it does suggest that actively dissolving interfaces may display a fractal geometry, in line with previous observations on stylolite interfaces. To further validate the model, the characteristics of such interfaces need to be better constrained.
3. The new models for pressure solution concurrent with grain boundary evolution provide means to investigate long-term compaction behavior of relatively pure (monophase) natural aggregates under in situ conditions. However, the driving force for grain boundary evolution provided by differences in solid-solid and solid-liquid surface energy may be diminished or absent bimineral interfaces, so that polyphase aggregates may not exhibit a pronounced retardation of pressure solution creep rates as seen in monophase aggregates. This is of particular interest to the investigation of interseismic restrengthening of gouge-filled faults, which often feature a heterogeneous mineralic composition.

Our model for pressure solution concurrent with structural evolution of the grain boundary provides new insights into the process of pressure solution and demonstrates the relevance of explicitly considering the structure of a wetted grain contact under stress. This warrants future research into the structure dynamics and evolution of grain boundaries in stressed fluid-rock systems in greater detail.

Table A1
Summary of Experimental Parameters Reported by Schutjens (1991)

Test no.	Grain size (μm)	Initial porosity (%)	Final porosity (%)
L1	50–75	40.2	2.3
L2	75–106	39.9	4.3
L3	106–125	39.1	3.6
L4	125–150	39.2	6.3

*Note.*The sample material was sieved to the reported grain size range, and the (instantaneous) porosities were estimated based on measured volumetric changes of the sample.

Appendix A: Laboratory Procedure of Schutjens (1991)

In the laboratory experiments performed by Schutjens (1991), the sample material was prepared from a batch of analytical grade granular halite (NaCl; Merck Chemical Company) which was double sieved to the desired grain size fractions. The samples were created by funneling the granular halite into latex balloon membranes, which were subsequently inflated and slowly deflated to form well-rounded samples with an average diameter of 5.5±0.5 cm. Next, the balloons were sealed around a stainless steel pore fluid pipe that was terminated by a permeable end cap, and the assembly was mounted inside a silicone oil medium hydrostatic pressure vessel. The pressure in this vessel was servocontrolled within 0.01 MPa, and volumetric changes in the sample were measured using a system of burettes connected to the pore fluid pipe. With this system, volumetric strain rates down to 10×10^{-9} s^{-1} could be resolved. Data were recorded manually, with 42 data points measured over the duration of the experiments. All compaction tests were carried out at room temperature conditions. First, the sample was loaded dry up to 2.15 MPa and precompacted for a duration of about 30 min, after which the pressure was lowered to a value of 0.05 MPa to keep the balloon membrane pressed against the sample. The pore fluid was subsequently introduced by vacuum flushing. Finally, the vessel was pressurized to a target effective pressure of 4.3 MPa, and the sample was allowed to compact over a duration of 21 days. The sample porosities were measured before and after the experiment using the Archimedes technique, and instantaneous porosities were estimated based on the sample volumetric changes while it was mounted in the apparatus. A total of four experiments was conducted, and their characteristics are displayed in Table A1.

Acknowledgments
M. v. d. E. would like to thank T. K. T. Wolterbeek for scientific discussion of the asperity growth model. This project is supported by the European Research Council (ERC), Grant 335915, by the NWO Vidi Grant 854.12.001 awarded to A. R. Niemeijer, and by the French Government through the UCA[JEDI] Investments in the Future project managed by the National Research Agency (ANR) with the Reference ANR-15-IDEX-01. This paper is theoretical and presents no new data. The sources of the laboratory data are cited in the main text.

References

Angevine, C. L., Turcotte, D. L., & Furnish, M. D. (1982). Pressure solution lithification as a mechanism for the stick-slip behavior of faults. *Tectonics*, *1*(2), 151–160. https://10.1130/10.1029/TC001i002p00151

Avnir, D., Farin, D., & Pfeifer, P. (1984). Molecular fractal surfaces. *Nature*, *308*(5956), 261–263. https://10.1130/10.1038/308261a0

Beeler, N. M., & Hickman, S. H. (2015). Direct measurement of asperity contact growth in quartz at hydrothermal conditions. *Journal of Geophysical Research: Solid Earth*, *120*, 3599–3616. https://10.1130/10.1002/2014JB011816

Blanpied, M. L., Lockner, D. A., & Byerlee, J. D. (1992). An earthquake mechanism based on rapid sealing of faults. *Nature*, *358*(6387), 574. https://10.1130/10.1038/358574a0

Bos, B., Peach, C. J., & Spiers, C. J. (2000). Slip behavior of simulated gouge-bearing faults under conditions favoring pressure solution. *Journal of Geophysical Research*, *105*(B7), 16,699–16,717. https://10.1130/10.1029/2000JB900089

Brantley, S. L. (1992). The effect of fluid chemistry on quartz microcrack lifetimes. *Earth and Planetary Science Letters*, *113*(1-2), 145–156. https://10.1130/10.1016/0012-821X(92)90216-I

Brodsky, E. E., Kirkpatrick, J. D., & Candela, T. (2016). Constraints from fault roughness on the scale-dependent strength of rocks. *Geology*, *44*(1), 19–22. https://10.1130/10.1130/G37206.1

Brown, S. R., & Scholz, C. H. (1985). Closure of random elastic surfaces in contact. *Journal of Geophysical Research*, *90*(B7), 5531–5545. https://10.1130/10.1029/JB090iB07p05531

Candela, T., Renard, F., Klinger, Y., Mair, K., Schmittbuhl, J., & Brodsky, E. E. (2012). Roughness of fault surfaces over nine decades of length scales. *Journal of Geophysical Research*, *117*, B08409. https://10.1130/10.1029/2011JB009041

Chen, J., & Spiers, C. J. (2016). Rate and state frictional and healing behavior of carbonate fault gouge explained using microphysical model. *Journal of Geophysical Research: Solid Earth*, *121*, 8642–8665. https://10.1130/10.1002/2016JB013470

Chester, F. M., & Chester, J. S. (1998). Ultracataclasite structure and friction processes of the Punchbowl fault, San Andreas system, California. *Tectonophysics*, *295*(1-2), 199–221. https://10.1130/10.1016/S0040-1951(98)00121-8

Croizé, D., Bjørlykke, K., Jahren, J., & Renard, F. (2010). Experimental mechanical and chemical compaction of carbonate sand. *Journal of Geophysical Research*, *115*, B11204. https://10.1130/10.1029/2010JB007697

de Boer, R., Nagtegaal, P., & Duyvis, E. (1977). Pressure solution experiments on quartz sand. *Geochimica et Cosmochimica Acta*, *41*(2), 257–264. https://10.1130/10.1016/0016-7037(77)90233-2

de Meer, S., Spiers, C. J., & Nakashima, S. (2005). Structure and diffusive properties of fluid-filled grain boundaries: An in-situ study using infrared (micro) spectroscopy. *Earth and Planetary Science Letters*, *232*(3-4), 403–414. https://10.1130/10.1016/j.epsl.2004.12.030

de Meer, S., Spiers, C. J., Peach, C. J., & Watanabe, T. (2002). Diffusive properties of fluid-filled grain boundaries measured electrically during active pressure solution. *Earth and Planetary Science Letters*, *200*(1), 147–157. https://10.1130/10.1016/S0012-821X(02)00585-X

Desbois, G., Urai, J. L., & de Bresser, J. H. (2012). Fluid distribution in grain boundaries of natural fine-grained rock salt deformed at low differential stress (Qom Kuh salt fountain, central Iran): Implications for rheology and transport properties. *Journal of Structural Geology*, *43*, 128–143. https://10.1130/10.1016/j.jsg.2012.07.002

Dewers, T., & Hajash, A. (1995). Rate laws for water-assisted compaction and stress-induced water-rock interaction in sandstones. *Journal of Geophysical Research*, *100*(B7), 13,093–13,112. https://10.1130/10.1029/95JB00912

Dieterich, J. H., & Kilgore, B. D. (1996). Imaging surface contacts: Power law contact distributions and contact stresses in quartz, calcite, glass and acrylic plastic. *Tectonophysics*, *256*(1-4), 219–239. https://10.1130/10.1016/0040-1951(95)00165-4

Elliott, D. (1973). Diffusion flow laws in metamorphic rocks. *GSA Bulletin*, *84*(8), 2645–2664. https://doi.org/10.1130/0016-7606(1973)84<2645:DFLIMR>2.0.CO;2

Evans, J. P., & Chester, F. M. (1995). Fluid-rock interaction in faults of the San Andreas system: Inferences from San Gabriel fault rock geochemistry and microstructures. *Journal of Geophysical Research*, *100*(B7), 13,007–13,020. https://10.1130/10.1029/94JB02625

Ghoussoub, J., & Leroy, Y. M. (2001). Solid-phase transformation within grain boundaries during compaction by pressure solution. *Journal of the Mechanics and Physics of Solids*, *49*(10), 2385–2430. https://10.1130/10.1016/S0022-5096(01)00012-6

Gratier, J. P. (1987). Pressure solution-deposition creep and associated tectonic differentiation in sedimentary rocks. *Geological Society, London, Special Publications*, *29*(1), 25–38. https://10.1130/10.1144/GSL.SP.1987.029.01.03

Gratier, J. P., Dysthe, D. K., & Renard, F. (2013). The role of pressure solution creep in the ductility of the Earth's upper crust, *Advances in Geophysics* (vol. 54, pp. 47–179): Elsevier. https://10.1130/10.1016/B978-0-12-380940-7.00002-0

Gratier, J. P., Guiguet, R., Renard, F., Jenatton, L., & Bernard, D. (2009). A pressure solution creep law for quartz from indentation experiments. *Journal of Geophysical Research*, *114*, B03403. https://10.1130/10.1029/2008JB005652

Gratier, J., Muquet, L., Hassani, R., & Renard, F. (2005). Experimental microstylolites in quartz and modeled application to natural stylolitic structures. *Journal of Structural Geology*, *27*(1), 89–100. https://10.1130/10.1016/j.jsg.2004.05.007

Heald, M. T. (1955). Stylolites in sandstones. *The Journal of Geology*, *63*(2), 101–114.

Hickman, S. H., & Evans, B. (1991). Experimental pressure solution in halite: The effect of grain/interphase boundary structure. *Journal of the Geological Society*, *148*(3), 549–560. https://10.1130/10.1144/gsjgs.148.3.0549

Hickman, S. H., & Evans, B. (1992). Chapter 10 growth of grain contacts in halite by solution-transfer: Implications for diagenesis, lithification, and strength recovery, *International geophysics* (vol. 51, pp. 253–280): Elsevier. https://doi.org/10.1016/S0074-6142(08)62825-9

Holdsworth, R., van Diggelen, E., Spiers, C., de Bresser, J., Walker, R., & Bowen, L. (2011). Fault rocks from the SAFOD core samples: Implications for weakening at shallow depths along the San Andreas Fault, California. *Journal of Structural Geology*, *33*(2), 132–144. https://10.1130/10.1016/j.jsg.2010.11.010

Holness, M. B. (1992). Equilibrium dihedral angles in the system quartz-CO_2-H_2O-NaCl at 800°C and 1–15 kbar: The effects of pressure and fluid composition on the permeability of quartzites. *Earth and Planetary Science Letters*, *114*(1), 171–184. https://10.1130/10.1016/0012-821X(92)90159-S

Israelachvili, J. N. (1986). Measurement of the viscosity of liquids in very thin films. *Journal of Colloid and Interface Science*, *110*(1), 263–271. https://10.1130/10.1016/0021-9797(86)90376-0

Jefferies, S., Holdsworth, R., Wibberley, C., Shimamoto, T., Spiers, C., Niemeijer, A., & Lloyd, G.(2006). The nature and importance of phyllonite development in crustal-scale fault cores: An example from the Median Tectonic Line, Japan. *Journal of Structural Geology*, *28*(2), 220–235. https://10.1130/10.1016/j.jsg.2005.10.008

Jones, E., Oliphant, T., Peterson, P., et al. (2001). SciPy: Open source scientific tools for Python. https://www.scipy.org/

Karner, S. L., Chester, F. M., Kronenberg, A. K., & Chester, J. S. (2003). Subcritical compaction and yielding of granular quartz sand. *Tectonophysics*, *377*(3-4), 357–381. https://10.1130/10.1016/j.tecto.2003.10.006

Karner, S. L., Marone, C., & Evans, B. (1997). Laboratory study of fault healing and lithification in simulated fault gouge under hydrothermal conditions. *Tectonophysics*, *277*(1-3), 41–55. https://10.1130/10.1016/S0040-1951(97)00077-2

Lehner, F. K. (1990). Thermodynamics of rock deformation by pressure solution. In D. J. Barber, & P. G. Meredith (Eds.), *Deformation processes in minerals, ceramics and rocks* pp. 296–333). Dordrecht: Springer Netherlands. https://10.1130/10.1007/978-94-011-6827-4_12

Lehner, F. K. (1995). A model for intergranular pressure solution in open systems. *Tectonophysics*, *245*(3-4), 153–170. https://10.1130/10.1016/0040-1951(94)00232-X

Lehner, F. K., & Bataille, J. (1985). Nonequilibrium thermodynamics of pressure solution. *Pure and Applied Geophysics PAGEOPH*, *122*(1), 53–85. https://10.1130/10.1007/BF00879649

Lewis, S., & Holness, M. (1996). Equilibrium halite-H_2O dihedral angles: High rock-salt permeability in the shallow crust? *Geology*, *24*(5), 431–434. https://10.1130/10.1130/0091-7613(1996)024<0431:EHHODA>2.3.CO;2

Majumdar, A., & Tien, C. L. (1990). Fractal characterization and simulation of rough surfaces. *Wear*, *136*(2), 313–327. https://10.1130/10.1016/0043-1648(90)90154-3

Niemeijer, A., Elsworth, D., & Marone, C. (2009). Significant effect of grain size distribution on compaction rates in granular aggregates. *Earth and Planetary Science Letters*, *284*(3-4), 386–391. https://10.1130/10.1016/j.epsl.2009.04.041

Niemeijer, A. R., & Spiers, C. J. (2002). Compaction creep of quartz-muscovite mixtures at 500°C: Preliminary results on the influence of muscovite on pressure solution. *Geological Society, London, Special Publications*, *200*(1), 61–71. https://10.1130/10.1144/GSL.SP.2001.200.01.04

Niemeijer, A., & Spiers, C. (2006). Velocity dependence of strength and healing behaviour in simulated phyllosilicate-bearing fault gouge. *Tectonophysics*, *427*(1-4), 231–253. https://10.1130/10.1016/j.tecto.2006.03.048

Niemeijer, A., Spiers, C., & Bos, B. (2002). Compaction creep of quartz sand at 400-600°C: Experimental evidence for dissolution-controlled pressure solution. *Earth and Planetary Science Letters*, *195*(3-4), 261–275. https://10.1130/10.1016/S0012-821X(01)00593-3

Pluymakers, A. M. H., & Spiers, C. J. (2015). Compaction creep of simulated anhydrite fault gouge by pressure solution: Theory v. experiments and implications for fault sealing. *Geological Society, London, Special Publications*, *409*(1), 107–124. https://10.1130/10.1144/SP409.6

Raj, R. (1982). Creep in polycrystalline aggregates by matter transport through a liquid phase. *Journal of Geophysical Research*, *87*(B6), 4731–4739. https://10.1130/10.1029/JB087iB06p04731

Ramm, M. (1992). Porosity-depth trends in reservoir sandstones: Theoretical models related to Jurassic sandstones offshore Norway. *Marine and Petroleum Geology*, *9*(5), 553–567. https://10.1130/10.1016/0264-8172(92)90066-N

Renard, F., Beauprêtre, S., Voisin, C., Zigone, D., Candela, T., Dysthe, D. K., & Gratier, J. P. (2012). Strength evolution of a reactive frictional interface is controlled by the dynamics of contacts and chemical effects. *Earth and Planetary Science Letters*, *341-344*, 20–34. https://10.1130/10.1016/j.epsl.2012.04.048

Renard, F., Schmittbuhl, J., Gratier, J. P., Meaking, P., & Merino, E. (2004). Three-dimensional roughness of stylolites in limestones. *Journal of Geophysical Research*, *109*, B03209. https://10.1130/10.1029/2003JB002555

Robin, P. Y. F. (1978). Pressure solution at grain-to-grain contacts. *Geochimica et Cosmochimica Acta*, *42*(9), 1383–1389. https://10.1130/10.1016/0016-7037(78)90043-1

Rutter, E. H. (1983). Pressure solution in nature, theory and experiment. *Journal of the Geological Society*, *140*(5), 725–740. https://10.1130/10.1144/gsjgs.140.5.0725

Rutter, E. H., & Elliott, D. (1976). The kinetics of rock deformation by pressure solution [and discussion]. *Philosophical Transactions of the Royal Society of London. Series A, Mathematical and Physical Sciences*, *283*(1312), 203–219.

Sahimi, M. (2003). *Heterogeneous materials I: Linear transport and optical properties*. New York: Springer-Verlag.

Schmittbuhl, J., Renard, F., Gratier, J. P., & Toussaint, R. (2004). Roughness of stylolites: Implications of 3D high resolution topography measurements. *Physical Review Letters*, *93*(23), 238501. https://10.1130/10.1103/PhysRevLett.93.238501

Schutjens, P. M. T. M. (1991). *Intergranular pressure solution in halite aggregates and quartz sands: An experimental investigation*. Utrecht: Utrecht University.

Schutjens, P. M. T. M., & Spiers, C. J. (1999). Intergranular pressure solution in Nacl: Grain-to-grain contact experiments under the optical microscope. *Oil & Gas Science and Technology*, *54*(6), 729–750. https://10.1130/10.2516/ogst:1999062

Shanhua, X., Songbo, R., & Youde, W. (2015). Three-dimensional surface parameters and multi-fractal spectrum of corroded steel. *PLOS ONE*, *10*(6), e0131361. https://10.1130/10.1371/journal.pone.0131361

Shimizu, I. (1995). Kinetics of pressure solution creep in quartz: Theoretical considerations. *Tectonophysics*, *245*(3-4), 121–134. https://10.1130/10.1016/0040-1951(94)00230-7

Sleep, N. H., & Blanpied, M. L. (1992). Creep, compaction and the weak rheology of major faults. *Nature*, *359*(6397), 687–692. https://10.1130/10.1038/359687a0

Smeraglia, L., Bettucci, A., Billi, A., Carminati, E., Cavallo, A., Di Toro, G., et al. (2017). Microstructural evidence for seismic and aseismic slips along clay-bearing, carbonate faults. *Journal of Geophysical Research: Solid Earth*, *122*, 3895–3915. https://10.1130/10.1002/2017JB014042

Spiers, C. J., de Meer, S., Niemeijer, A. R., & Zhang, X. (2004). Kinetics of rock deformation by pressure solution and the role of thin aqueous films. In S. Nakashima (Ed.), *Physicochemistry of Thin Film Mater* pp. 129–158). Tokyo: Universal Academy Press.

Spiers, C. J., & Schutjens, P. M. T. M. (1990). Densification of crystalline aggregates by fluid-phase diffusional creep. In D. J. Barber, & P. G. Meredith (Eds.), *Deformation Processes in Minerals, Ceramics and Rocks* pp. 334–353). Dordrecht: Springer Netherlands. https://10.1130/10.1007/978-94-011-6827-4_13

Spiers, C. J., Schutjens, P. M. T. M., Brzesowsky, R. H., Peach, C. J., Liezenberg, J. L., & Zwart, H. J. (1990). Experimental determination of constitutive parameters governing creep of rocksalt by pressure solution. *Geological Society, London, Special Publications*, *54*(1), 215–227. https://10.1130/10.1144/GSL.SP.1990.054.01.21

Stauffer, D., & Aharony, A. (1992). *Introduction to percolation theory* (2nd ed.). London: Taylor & Francis.

Stöckhert, B., Wachmann, M., Küster, M., & Bimmermann, S. (1999). Low effective viscosity during high pressure metamorphism due to dissolution precipitation creep: The record of HP-LT metamorphic carbonates and siliciclastic rocks from Crete. *Tectonophysics*, *303*(1-4), 299–319. https://10.1130/10.1016/S0040-1951(98)00262-5

Tada, R., & Siever, R. (1989). Pressure solution during diagenesis. *Annual Review of Earth and Planetary Sciences*, *17*(1), 89–118. https://10.1130/10.1146/annurev.ea.17.050189.000513

Urai, J. L., Spiers, C. J., Zwart, H. J., & Lister, G. S. (1986). Weakening of rock salt by water during long-term creep. *Nature*, *324*(6097), 554. https://10.1130/10.1038/324554a0

van Noort, R., Spiers, C. J., & Pennock, G. M. (2008). Compaction of granular quartz under hydrothermal conditions: Controlling mechanisms and grain boundary processes. *Journal of Geophysical Research*, *113*, B12206. https://10.1130/10.1029/2008JB005815

van Noort, R., Visser, H. J. M., & Spiers, C. J. (2008). Influence of grain boundary structure on dissolution controlled pressure solution and retarding effects of grain boundary healing. *Journal of Geophysical Research*, *113*, B03201. https://10.1130/10.1029/2007JB005223

van den Ende, M. P. A., Marketos, G., Niemeijer, A. R., & Spiers, C. J. (2018). Investigating compaction by intergranular pressure solution using the discrete element method. *Journal of Geophysical Research: Solid Earth*, *123*, 107–124. https://10.1130/10.1002/2017JB014440

van den Ende, M. P. A., & Niemeijer, A. R. (2019). An investigation into the role of time-dependent cohesion in interseismic fault restrengthening. *Scientific Reports*, *9*, 9894. https://10.1130/10.1038/s41598-019-46241-5

Visser, H. J. M. (1999). *Mass transfer processes in crystalline aggregates containing a fluid phase*. Utrecht: Utrecht University.

Wong, P. z., Howard, J., & Lin, J. S. (1986). Surface roughening and the fractal nature of rocks. *Physical Review Letters*, *57*(5), 637–640. https://10.1130/10.1103/PhysRevLett.57.637

Yasuhara, H., Marone, C., & Elsworth, D. (2005). Fault zone restrengthening and frictional healing: The role of pressure solution. *Journal of Geophysical Research*, *110*, B06310. https://10.1130/10.1029/2004JB003327

Zahouani, H., Vargiolu, R., & Loubet, J. L. (1998). Fractal models of surface topography and contact mechanics. *Mathematical and Computer Modelling*, *28*(4), 517–534. https://10.1130/10.1016/S0895-7177(98)00139-3

Zhang, X., Spiers, C. J., & Peach, C. J. (2010). Compaction creep of wet granular calcite by pressure solution at 28°C to 150°C. *Journal of Geophysical Research*, *115*, B09217. https://10.1130/10.1029/2008JB005853

Zubtsov, S., Renard, F., Gratier, J. P., Guiguet, R., Dysthe, D. K., & Traskine, V. (2004). Experimental pressure solution compaction of synthetic halite/calcite aggregates. *Tectonophysics*, *385*(1-4), 45–57. https://10.1130/10.1016/j.tecto.2004.04.016